Self-consistent feedback mechanism for the sudden viscous dissipation of finite-Mach-number compressing turbulence

Alejandro Campos and Brandon E. Morgan

Self-consistent feedback mechanism for the sudden viscous dissipation of finite-Mach-number compressing turbulence

Alejandro Campos* and Brandon E. Morgan
Lawrence Livermore National Laboratory, Livermore, California 94550, USA
(Dated:)

Previous work (S. Davidovits and N. J. Fisch, "Sudden viscous dissipation of compressing turbulence," Phys. Rev. Lett., 116(105004), 2016) demonstrated that the compression of a turbulent field can lead to a sudden viscous dissipation of turbulent kinetic energy (TKE), and suggested this mechanism could potentially be used to design new fast-ignition schemes for inertial confinement fusion (ICF). We expand on previous work by accounting for finite Mach numbers, rather than relying on a zero-Mach-limit assumption as previously done. The finite-Mach-number formulation is necessary to capture a self-consistent feedback mechanism in which dissipated TKE increases the temperature of the system, which in turn modifies the viscosity and thus the TKE dissipation itself. Direct numerical simulations with a tenth-order accurate Padé scheme were carried out to analyze this self-consistent feedback loop for compressing turbulence. Results show that, for finite Mach numbers, the sudden viscous dissipation of TKE still occurs, both for the solenoidal and dilatational turbulent fields. As the domain is compressed, oscillations in dilatational TKE are encountered due to the highly-oscillatory nature of the pressure dilatation. An analysis of the source terms for the internal energy shows that the mechanical-work term dominates the viscous turbulent dissipation. As a result, the effect of the suddenly dissipated TKE on temperature is minimal for the Mach numbers tested. Moreover, an analytical expression is derived that confirms the dissipated TKE does not significantly alter the temperature evolution for low Mach numbers, regardless of compression speed. The self-consistent feedback mechanism is thus quite weak for subsonic turbulence, which could limit its applicability for ICF.

I. INTRODUCTION

The compression of a turbulent flow occurs in a broad array of applications. Examples include one-dimensional compressions in internal combustion engines [1] or across shock waves [2], axisymmetric compressions in Z-pinches [3], spherically-symmetric compressions in inertial confinement fusion (ICF) [4, 5], and three-dimensional complex contractions in the interstellar medium [6]. Moreover, the compression mechanism often leads to complex turbulence dynamics, and the resulting evolution of turbulence can have a strong effect on the overall behavior of the application under consideration. Thus, increased levels of understanding and improved modeling capabilities for this phenomenon are essential.

Numerous direct numerical simulations of compressing turbulence have been previously carried out with the aim of improving engineering turbulence models; see for example [7–11]. These studies treated the fluid as a traditional gas, for which the dependence of viscosity μ on temperature T is given by $\mu \sim T^n$, with n having a value of, or close to, 3/4. On the other hand, [12] demonstrated, through computational simulations, that when a power law exponent characteristic of weakly-coupled plasmas is used, i.e. $n = 5/2$, a sudden viscous mechanism occurs which dissipates the turbulent energy. Their results showed that a turbulent field subjected to a continuous isotropic compression initially creates an amplification of turbulent kinetic energy (TKE), until viscous scaling dominates and TKE is rapidly dissipated into heat. It was thus proposed in [12] that the resulting increases of temperature could be used to improve the ignition conditions for ICF.

Subsequent work has expanded on the simulations of [12]. The effect of ionization on the scaling of viscosity was accounted for in [13]. For that study, the ionization state Z was assumed to depend solely on temperature, and thus the plasma viscosity $\mu \sim T^{5/2}/Z^4$ was simplified to the form $\mu \sim T^\beta$. Their analysis of the evolution of the energy spectrum showed that the sudden dissipation of TKE occurs for $\beta > 1$ only. A TKE model that accounts for the viscous dissipative mechanism for isotropic compressions is presented in [14]. This model was validated against direct numerical simulations, and showed excellent agreement for viscosity-power-law exponents greater than one. The model was then used to estimate the partition of energy between the turbulence and heat, as the compression proceeds in time. A two-point spectral model based on the

* campos33@llnl.gov

EDQNM formulation was used by [15], along with direct numerical simulations, to reproduce the sudden viscous dissipation mechanism. The lower computational cost of the EDQNM model allowed for the analysis of high-Reynolds-number effects and thus the identification of three distinct regimes: turbulent production, non-linear energy transfer, and viscous dissipation. Moreover, the assumption of homogeneous turbulence was relaxed and a spherical inhomogeneous turbulent layer under compression was simulated with both DNS and EDQNM closures. The sudden dissipation of TKE was also observed for this new case. Finally, in [16], a stability boundary for hot spot turbulence was derived to demarcate states of the compression for which a decrease of TKE is guaranteed. Moreover, an upper limit for the amount of TKE that can be generated during a compression was proposed. This upper limit was then compared to the internal thermal energy of the system.

The simulations of the sudden viscous dissipation mechanism previously conducted have relied on the zero-Mach-limit assumption. Given a decomposition of the velocity $U_i = \langle U_i \rangle + u_i$, where $\langle U_i \rangle$ is the Reynolds-averaged mean flow and u_i the fluctuating velocity, the governing equations for the fluctuations in the zero-Mach limit take the form [7]

$$\frac{\partial u_i}{\partial x_i} = 0, \qquad (1)$$

$$\langle \rho \rangle \left(\frac{\partial u_i}{\partial t} + u_j \frac{\partial u_i}{\partial x_j} \right) = -\frac{\partial P}{\partial x_i} + \mu \frac{\partial^2 u_i}{\partial x_j \partial x_j} + f_i. \qquad (2)$$

In the above, $\langle \rho \rangle$ is the Reynolds-averaged density, P the pressure, μ the viscosity, and f_i a forcing function that accounts for the effect of the compression. The viscosity depends on temperature and thus an a-priori time evolution for temperature needs to be provided. For an adiabatic isotropic compression, this is

$$T = T_0 L^{-2}, \qquad (3)$$

where L is a characteristic length of the domain being compressed and T_0 the initial temperature.

The approach described above is suitable for demonstrating the sudden dissipation of TKE, but does not capture the self-consistent feedback mechanism mentioned in [12]. This mechanism begins with a self-consistent energy transfer from the TKE towards the internal energy, as a result of the sudden viscous dissipation. This, in turn, causes increased temperatures that amplify the viscosity of the system. The stronger values of viscosity then precipitate the viscous dissipation of TKE, thus completing a feedback loop. In the zero-Mach limit, an evolution equation for the internal energy is not solved, and thus the effect of the dissipated TKE on the internal energy and the viscosity cannot be reproduced in a self-consistent fashion. It is expected that accounting for the feedback mechanism would lead to viscous dissipations that are more sudden, or of increased intensity [12]. An alternative to the assumption of the zero-Mach limit is turbulence belonging to the finite-Mach number regime. For this case, fully coupled governing equations for density, velocity, and energy are solved, which allows for an explicit accounting of the forward transfer of dissipated TKE into heat, and the subsequent effect of increased temperature and viscosity on the dissipation. The focus of this study is the simulation of turbulence in the finite-Mach number regime to investigate the complex self-consistent feedback mechanism, and thus further assess the benefits of viscous dissipation for ICF and other high-energy density applications.

The outline of the paper is as follows. Section II includes a description of the governing equations for turbulence in the finite-Mach number regime. The mechanisms that account for the energy transfer between the TKE and the internal energy are also discussed. In Section III, details of the numerical simulations, such as the discretization scheme and the creation of realistic initial conditions, are included. The results of the simulations are then provided in Section IV, which is divided into two subsections. Section IV A focuses on the component of the feedback mechanism related to the TKE. Thus, the evolution of the TKE, its budget, and spectra are analyzed in this subsection. The component of the feedback loop associated with the internal energy is then investigated in Section IV B, where an analysis of the temperature evolution and sources for the internal energy are included. Finally, the paper ends with Section V, where concluding remarks and a discussion of future work is provided.

II. GOVERNING EQUATIONS

A. Navier-Stokes equations for isotropic compressions

We denote $\widetilde{U}_i$ and u_i'' as the Favre-averaged and Favre-fluctuating velocities, respectively, so that

$U_i = \widetilde{U}_i + u_i''$ [17]. In analogy to the zero-Mach-limit formulation of [12], we analyze the effect of a compression on a statistically homogeneous turbulent field u_i'', where the compression is achieved through a specified Favre-averaged mean flow $\widetilde{U}_i$. The Favre-averaged velocity for homogeneous compressible turbulence needs to be restricted to the form $\widetilde{U}_i = G_{ij}x_j$ [9]. The deformation tensor G_{ij} corresponding to an isotropic compression is given in [7, 9, 12], and can be expressed as

$$G_{ij} = \frac{\dot{L}}{L}\delta_{ij}, \tag{4}$$

where L is a time-dependent characteristic length of the compressed domain, and $\dot{L}$ is the constant time rate of change of L. Given this formalism, one can derive, as detailed in Appendix A, a set of Navier-Stokes equations for the fluctuating velocity undergoing mean-flow compression. These equations, which are summarized below, constitute the finite-Mach-number analog of the low-Mach-number Eqs. (1) to (3),

$$\frac{\partial \rho}{\partial t} + \frac{\partial \rho u_i''}{\partial x_i} = f^{(\rho)}, \tag{5}$$

$$\frac{\partial \rho u_i''}{\partial t} + \frac{\partial \rho u_i'' u_j''}{\partial x_j} = \frac{\partial \sigma_{ij}}{\partial x_j} + f_i^{(u)}, \tag{6}$$

$$\frac{\partial \rho E_t}{\partial t} + \frac{\partial \rho E_t u_i''}{\partial x_i} = \frac{\partial u_i'' \sigma_{ij}}{\partial x_j} + \frac{\partial}{\partial x_j}\left(\kappa \frac{\partial T}{\partial x_j}\right) + f^{(e)}. \tag{7}$$

In the above ρ is the density, u_i'' the Favre-fluctuating velocity, and T the temperature. E_t is the total energy, which is given by $E_t = U + K_t$, where $U = C_v T$ is the internal energy and $K_t = \frac{1}{2}u_i'' u_i''$ is the kinetic energy associated with the turbulent fluctuations. C_v is the specific heat at constant volume. The stress tensor is given by

$$\sigma_{ij} = -P\delta_{ij} + 2\mu\left[\frac{1}{2}\left(\frac{\partial u_i''}{\partial x_j} + \frac{\partial u_j''}{\partial x_i}\right) - \frac{1}{3}\frac{\partial u_k''}{\partial x_k}\delta_{ij}\right], \tag{8}$$

where P is the pressure and μ the viscosity. A power law of the form $\mu = \mu_0 (T/T_0)^n$ is used, where μ_0 and T_0 represent reference viscosity and temperature values, and n is the power-law exponent. The thermal conductivity κ is computed according to $\kappa = \mu C_p / Pr$, where C_p is the specific heat at constant pressure and Pr the Prandtl number. An ideal equation of state $P = \rho R T$ is used, where R is the

ideal gas constant. The forcing functions $f^{(\rho)}$, $f_i^{(u)}$, and $f^{(e)}$ account for the effect of the mean compression on the density, velocity, and total energy, respectively, and are defined as

$$f^{(\rho)} = -2\dot{L}\rho, \tag{9}$$

$$f_i^{(u)} = -3\dot{L}\rho u_i'', \tag{10}$$

$$f^{(e)} = -\left[2\rho E_t + \rho u_i'' u_i'' + 3P\right]\dot{L}. \tag{11}$$

The equations above are suitable for numerical simulations now that the compressive effect of the mean flow $\widetilde{U}_i$ has been abstracted into the three forcing functions above. These are the equations solved for the current study.

B. Energy exchange for compressible turbulence

For turbulence in the finite-Mach-number regime, the Helmholtz decomposition is often employed to express the fluctuating velocity as $u_i'' = u_i''^{(s)} + u_i''^{(d)}$, where $u_i''^{(s)}$ and $u_i''^{(d)}$ are the solenoidal and dilatational velocities, respectively. The solenoidal component satisfies $\nabla \times \mathbf{u}''^{(s)} = \mathbf{w}$ and $\nabla \cdot \mathbf{u}''^{(s)} = 0$, where $\mathbf{w} = \nabla \times \mathbf{u}''$ is the vorticity vector, and the dilatational component satisfies $\nabla \times \mathbf{u}''^{(d)} = 0$ and $\nabla \cdot \mathbf{u}''^{(d)} = d$, where $d = \nabla \cdot \mathbf{u}''$ is the dilatation.

Given this decomposition, two TKEs can be defined. These are the solenoidal TKE

$$k^{(s)} = \frac{1}{2}\widetilde{u_i''^{(s)} u_i''^{(s)}}, \tag{12}$$

the dilatational TKE

$$k^{(d)} = \frac{1}{2}\widetilde{u_i''^{(d)} u_i''^{(d)}}. \tag{13}$$

There are two additional energies in the system, namely, the mean kinetic energy

$$\bar{K} = \frac{1}{2}\widetilde{U}_i\widetilde{U}_i, \tag{14}$$

and the mean internal energy

$$\widetilde{U} = C_v\widetilde{T}. \tag{15}$$

The governing equations for the solenoidal and dilatational TKEs given a non-zero mean flow can be derived following the procedure of [18]. Along with

3

TABLE I: Sources in the evolution equations for the solenoidal, dilatational, mean, and internal energies. Upper scripts α stand for either s or d. τ_{ij} represents the Favre-averaged Reynolds stresses ($\tau_{ij} = \widetilde{u_i'' u_j''}$).

Name	Symbol	Definition
Intermode advection	$IA^{(\alpha)}$	$-\left\langle \frac{\partial \sqrt{\rho} u_j''}{\partial x_j} \sqrt{\rho} u_i''^{(\alpha)} \right\rangle + \left\langle \frac{\rho u_i'' u_i''^{(\alpha)}}{2} d \right\rangle$
Production	$P^{(\alpha)}$	$-\frac{2}{3} \langle \rho \rangle k^{(\alpha)} G_{ii}$
Solenoidal dissipation	$\langle \rho \rangle \epsilon^{(s)}$	$\langle \mu w_i w_i \rangle$
Dilatational dissipation	$\langle \rho \rangle \epsilon^{(d)}$	$\frac{4}{3} \langle \mu d^2 \rangle$
Pressure dilatation	PD	$\langle Pd \rangle$
Mean kinetic energy advection	$AD^{(\bar{K})}$	$\langle \rho \rangle \widetilde{U}_j \frac{\partial \bar{K}}{\partial x_j}$
Mean kinetic energy transport	$T^{(\bar{K})}$	$\frac{\partial}{\partial x_j} \left(\widetilde{U}_i \langle \rho \rangle \tau_{ij} + \widetilde{U}_j \langle P \rangle \right)$
Mechanical work	MW	$-\langle P \rangle G_{ii}$

the evolution equations for $\bar{K}$ and $\widetilde{U}$, one can summarize the governing dynamics of the four relevant energies for homogeneous turbulence as follows

$$\langle \rho \rangle \frac{dk^{(s)}}{dt} = IA^{(s)} + P^{(s)} - \langle \rho \rangle \epsilon^{(s)}, \qquad (16)$$

$$\langle \rho \rangle \frac{dk^{(d)}}{dt} = IA^{(d)} + P^{(d)} - \langle \rho \rangle \epsilon^{(d)} + PD, \qquad (17)$$

$$\langle \rho \rangle \frac{\partial \bar{K}}{\partial t} = -AD^{(\bar{K})} - T^{(\bar{K})} - MW - P^{(s)} - P^{(d)}, \qquad (18)$$

$$\langle \rho \rangle \frac{d\tilde{U}}{dt} = MW + \langle \rho \rangle \epsilon^{(s)} + \langle \rho \rangle \epsilon^{(d)} - PD. \qquad (19)$$

Each of the sources in the evolution equations above is defined in Table I. We note that the derivation of the evolution equations for the four energies assumed a generic yet isotropic deformation tensor G_{ij}, and neglected the averaged heat flux since for homogeneous turbulence the averaged temperature is uniform in space [9]. The intermode advection represents a transfer of energy from the solenoidal and dilatational modes, and thus satisfies $IA^{(s)} = -IA^{(d)}$. The production terms transfer the compression energy stored in the mean flow to the solenoidal and dilatational TKEs. The solenoidal and dilatational dissipations then transfer energy stored in the solenoidal and dilatational fields into heat. The pressure dilatation represents a two-way energy transfer between the mean internal energy and the dilatational TKE only, and the mechanical work transfers energy of the compression directly into heat. The mean-kinetic-energy advection and transport are not identically zero, unlike the case

for the other three energies. These various energy-transfer mechanisms are depicted in Fig. 1. We note that each energy component has a direct interaction with each of the other three energies. We also note that the driver for the interactions is the mean kinetic energy, since it has a predetermined time evolution that emulates the compression of the system. The other three energy components then respond in a self-consistent fashion to the time evolution of the mean kinetic energy. The self-consistent feedback mechanism for the sudden viscous dissipation relies on these complex interactions, and thus can only be represented using the finite-Mach-number formulation and not the low-Mach-number assumption.

III. COMPUTATIONAL DETAILS

Direct numerical simulations of Eqs. (5) to (7) are carried out with the Miranda code developed at the Lawrence Livermore National Laboratory. This solver employs a tenth-order accurate Padé scheme [19] for the discretization of the spatial derivatives, and a fourth-order, low-storage, five-step Runge-Kutta solver [20] for the temporal derivatives. An eighth-order compact filter is applied to the conserved variables ρ, $\rho u_i''$, and E_t after each substep of the Runge-Kutta scheme, for the purposes of stability.

Miranda relies on the artificial-fluid-property approach to stabilize shock waves and contact discontinuities. Thus, an artificial bulk viscosity β^* is introduced in the definition of the viscous stress tensor, and an artificial thermal conductivity κ^* is added to the thermal conductivity κ of the fluid. The artificial
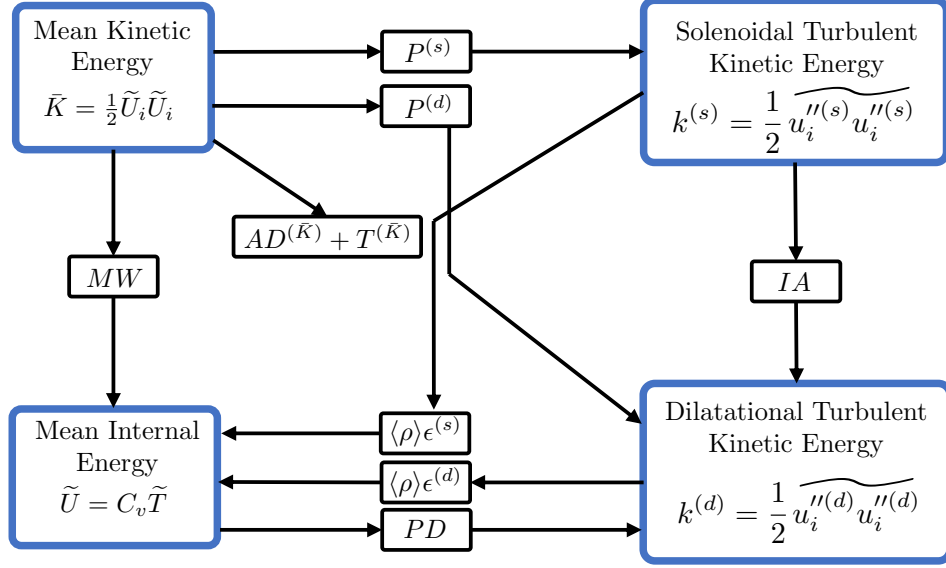
FIG. 1: Schematic of energy transfer between the four energy components: mean kinetic energy, mean internal energy, solenoidal TKE, and dilatational TKE.

bulk viscosity and artificial thermal conductivity are computed as

$$\beta^* = \overline{C_\beta \rho D(d)}, \tag{20}$$

$$\kappa^* = \overline{C_\kappa \rho \frac{c_v}{T \Delta t} D(T)}. \tag{21}$$

In the above, Δt is the time step, the overbar denotes a truncated-Gaussian filter, and $D(\cdot)$ is an eighth-order derivative operator defined as

$$D(\cdot) = \max\left(\left|\frac{\partial^8 \cdot}{\partial x^8}\right| \Delta x^{10}, \left|\frac{\partial^8 \cdot}{\partial y^8}\right| \Delta y^{10}, \left|\frac{\partial^8 \cdot}{\partial z^8}\right| \Delta z^{10}\right). \tag{22}$$

This operator strongly biases the artificial properties towards high wave numbers. The coefficients $C_\beta = 0.07$ and $C_\kappa = 0.001$ have been calibrated for simulations relevant to ICF—see for example [4, 21, 22]. For further details or capabilities of the code, the reader is referred to [23–25].

The computational domain consists of a cube of length 2π, with a uniform distribution of 256^3 grid points. Periodic boundary conditions are applied on all sides of the cube. The ratio of specific heats has a value of $\gamma = 5/3$, and the Prandtl number is set to $Pr = 1$. The gas constant is computed as $R = R_u/M$, where the universal gas constant is $R_u = 8.314474 \times 10^7$ (cgs units), and the molar mass used is that of Deuterium, i.e. $M = 2.014102$. Statistical quantities are obtained by averaging over all nodes of the mesh.

The initial flow field is extracted from a simulation of linearly-forced compressible turbulence [26, 27]. This preliminary simulation is carried out for a duration of 18 initial eddy-turn-over times. The forcing coefficients introduced in [26] require the specification of a priori values for the solenoidal and dilatational dissipations. These two quantities were obtained from specifying a total dissipation $\epsilon = \epsilon^{(s)} + \epsilon^{(d)}$ and a dissipation ratio $\epsilon^{(d)}/\epsilon^{(s)}$. As was done for the direct numerical simulations of [26], the value of the total dissipation was chosen a priori so that the corresponding Kolmogorov scale $\eta = (\nu^3/\epsilon)^{1/4}$ is sufficiently larger than the grid spac-
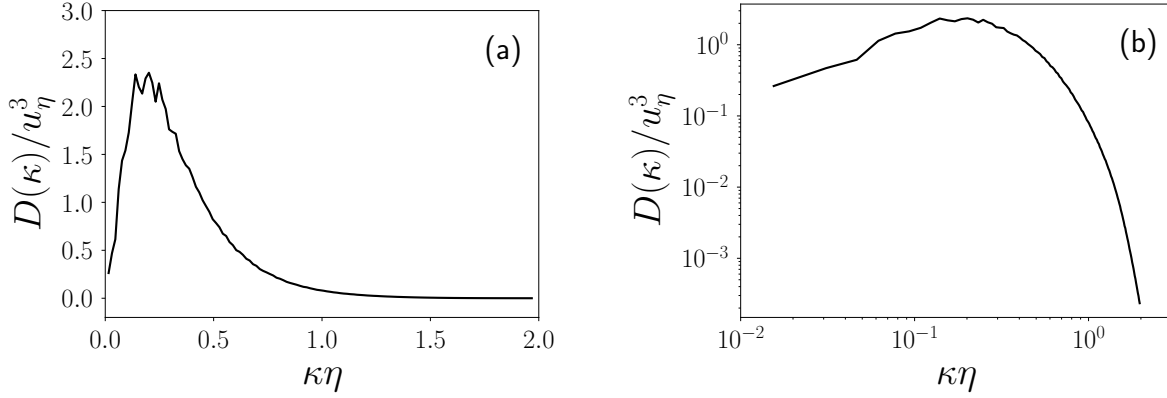
FIG. 2: The dissipation spectrum, normalized by the Kolmogorov velocity $u_\eta = (\epsilon\nu)^{1/4}$, at the final time of the linearly-forced simulation. Plots using a (a) linear scale and a (b) log-log scale are included.

ing and thus sufficient resolution is achieved. Using both a linear and a log-log scale, Fig. 2 shows the dissipation spectrum for the final time of the preliminary forced-turbulence simulation, and thus illustrates the range of scales resolved on the mesh, i.e. $0 \leq \kappa\eta \leq 2$. This figure shows that the simulations reproduce the long tail at high wavenumbers as it smoothly approaches a value of zero (compare Fig. 2(a) with fig. 6.16 of [28]), and a fictitious energy pileup or unphysical rapid decay at the highest wave numbers is avoided. This serves as further evidence that the chosen combination of forcing coefficients and mesh resolution appropriately capture all of the dissipative scales, as should be the case for any direct numerical simulation. The ratio of dissipations was set to $\epsilon^{(d)}/\epsilon^{(s)} = 0.01$. Simulations of compressing turbulence that were initialized from a linearly-forced case with $\epsilon^{(d)}/\epsilon^{(s)} = 1.0$ were also carried out. The results obtained with this larger initial dissipation ratio are qualitatively similar to those with an initial condition of $\epsilon^{(d)}/\epsilon^{(s)} = 0.1$, and the same conclusions regarding the self-consistent feedback mechanism are obtained. Thus this additional case is not included in this paper.

The turbulent Mach number and Taylor-scale Reynolds number are defined as

$$M_t = \frac{\sqrt{\widetilde{u_i'' u_i''}}}{\widetilde{c}}, \tag{23}$$

$$Re_\lambda = \left(\frac{20k^2}{3\epsilon\nu}\right)^{1/2}, \tag{24}$$

where $c = \sqrt{\gamma R T}$ is the speed of sound, and $\nu = \langle \mu \rangle / \langle \rho \rangle$ is the averaged kinematic viscosity. The extracted turbulent field at the end of the linear forcing has $M_t \approx 0.65$ and $Re_\lambda \approx 70$. The corresponding ratio of dilatational to solenoidal TKE is $k^{(d)}/k^{(s)} = 0.033$. For the linearly-forced simulations, the power law exponent is set to the traditional fluid value of $n = 3/4$. However, once the isotropic compression is applied to the initial flow field, the power law exponent is switched to the value used in [12], namely $n = 5/2$, so as to reproduce the sudden viscous dissipation mechanism. Thus, effects of the stronger power-law scaling have been isolated to the compressive phase only, and the linearly-forced simulations used the traditional fluid power-law exponent so as to have a standard turbulent flow field as the initial condition.

Once the compression starts the small scales will dissipate first, and only larger and larger scales will remain (see [12] and Fig. 9). Thus, if the initial condition is well resolved, then the flow field throughout the remainder of the simulated time will be well resolved as well. Whereas [12] stated that their simulations are initially under-resolved, but quickly become resolved as the compression progresses, for this case even the initial conditions are well-resolved, as described in the previous paragraph. An additional indication that the resolution improves as the compression proceeds is that the ratio of artificial dissipation [27] to physical dissipation, which has an already-low initial value of 0.016, decays rapidly as the compression is initiated. Thus, the simulations are mostly affected by physical rather than artificial

6

dissipative mechanisms, as should be the case for a properly-refined direct numerical simulation [25].

IV. RESULTS

The analysis of the self-consistent feedback mechanism is divided into two subsections. The first focuses on the behavior of the TKEs and the various mechanisms depicted in Fig. 1 that modulate their temporal evolution. The second half of the analysis is centered around the resulting evolution of the internal energy, and the amplification of the temperature due to the viscous dissipation.

A. Turbulent kinetic energies

1. Profile histories

The time evolution of the solenoidal and dilatational TKEs are shown in Figs. 3(a) and 3(b), respectively. As done in [12], rather than plotting the TKE evolution against time, a parameterization in terms of the length of the domain L is used, and thus time progresses from right to left. Also equivalent to the results in [12], the TKE evolutions for different compression speeds $\dot{L}$ are shown. These different cases are labelled by the initial value of the RDT parameter $S^* = Sk/\epsilon$, where $S = \dot{L}/L$ is the inverse time scale of the compression, and k/ϵ is the time scale of the turbulence. For sufficiently large values of S^*, the compression is rapid enough that the nonlinear turbulence-turbulence interactions are negligible, and the evolution of the turbulence is described exactly by rapid-distortion theory (RDT) [11, 28].

As Fig. 3 shows, it is not only the solenoidal but also the dilatational TKE that exhibits the sudden viscous dissipation mechanism of [12]. Even though the compression speeds used in this study are different from those of [12], there is strong qualitative agreement with the previously published results. The dilatational TKE is also in strong agreement with RDT [11] for the fastest compression rates. A notable difference to highlight for this new case is that increasingly strong oscillations of dilatational TKE appear as S_0^* is decreased. This highly oscillatory behavior is discussed further in Section IV A 2. Additionally, the dilatational energy has not decayed to values as low as those of the solenoidal TKE. For example, at the last recorded instance in time, the solenoidal TKE has decayed by more than three orders of magnitude for case $S_0^* = 500$, whereas the

dilatational TKE has decreased by less than two orders of magnitude. Lastly, for the slowest compression rate, the solenoidal and dilatational TKE diverge in their initial behavior: whereas the dilatational TKE slightly increases until it suddenly dissipates, the solenoidal TKE decreases from the start. As will be described in Section IV A 2, this is most likely due to the pressure dilatation acting as an energy source for the dilatational TKE.

An alternate representation of the evolution of TKEs is given in Figs. 4(a) and 4(b). In Fig. 4(a) the evolution of the solenoidal TKE is parameterized by the solenoidal shear parameter $S_s^* = Sk^{(s)}/\epsilon^{(s)}$, and in Fig. 4(b) the evolution of the dilatational TKE is parameterized by the dilatational shear parameter $S_d^* = Sk^{(d)}/\epsilon^{(d)}$. The dashed vertical lines correspond to the point in time at which production is equal to dissipation, that is, the point at which $P^{(s)} = \langle \rho \rangle \epsilon^{(s)}$ for Fig. 4(a) and $P^{(d)} = \langle \rho \rangle \epsilon^{(d)}$ for Fig. 4(b). The dashed diagonal lines correspond to the assumption of RDT scaling, for which $\epsilon^{(\alpha)} \sim \left(k^{(\alpha)}\right)^3$ for $\alpha = s, d$. That is, assuming this relationship between TKE and dissipation, the TKE can be expressed as

$$k^{(\alpha)} = \frac{\left(k^{(\alpha)}\right)^{3/2}}{\left(k^{(\alpha)}\right)^{1/2}} \sim \frac{\left(\epsilon^{(\alpha)}\right)^{1/2}}{\left(k^{(\alpha)}\right)^{1/2}} \sim S^{1/2} \, S_\alpha^{* \, -1/2} \quad (25)$$

for $\alpha = s, d$. It is important to note that $k^{(\alpha)}$ does not scale simply as $S_\alpha^{* \, -1/2}$ since S also depends on time. However, the dependence of S on time is given by the predetermined and known compression history of the domain L.

Fig. 4(a) shows that for compressions $S_0^* = 5.0$, 50, and 500, the initial increase in solenoidal TKE is in close agreement with the RDT scaling of Eq. (25), which could be beneficial for modeling purposes. Significant divergence from the RDT scaling occurs once the vertical line at which solenoidal production equals solenoidal dissipation is reached. After this point, the solenoidal dissipation overtakes the solenoidal production, and the turbulence decays. For the $S_0^* = 0.50$ case, the compression is slow enough that the solenoidal production is never larger than the solenoidal dissipation, and thus the entire curve is located to the left of the vertical dashed line. Fig. 4(b) shows a similar trend. We first note that the rapid oscillations in the dilatational profiles corresponding to slow compression speeds are also evident in this figure. The agreement with the RDT scaling still holds for the $S_0^* = 5.0, 50,$ and 500 cases, although, for the $S_0^* = 5.0$ case, this agreement is not as strong as that of the corresponding
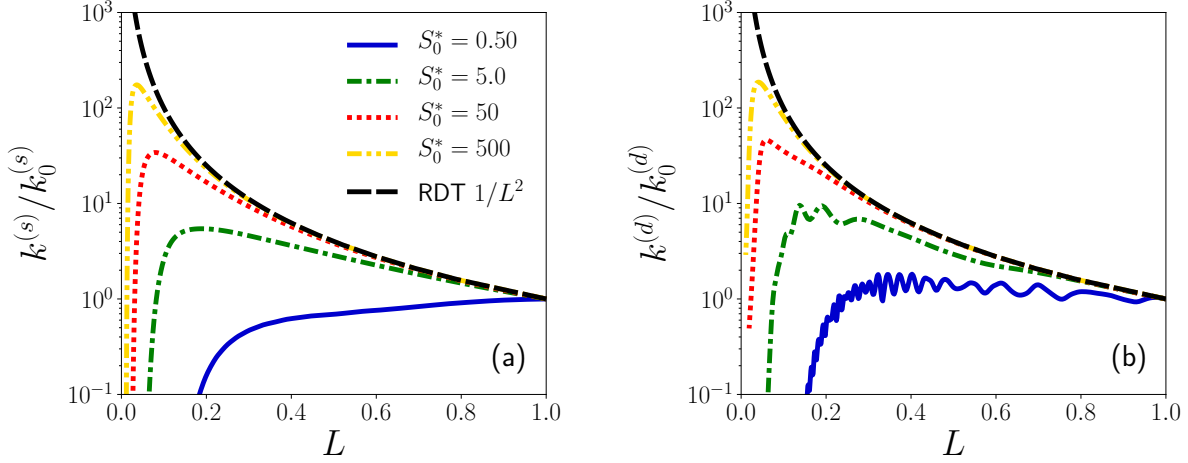
FIG. 3: Evolution of (a) solenoidal and (b) dilatational TKE as a function of the size of the domain L. S_0^* is the initial value of the shear parameter $S^* = Sk/\epsilon$, where $S = \dot{L}/L$. $k_0^{(s)}$ and $k_0^{(d)}$ are the initial values of $k^{(s)}$ and $k^{(d)}$, respectivley. The initial length of the domain is $L = 1$, which decreases as time progresses.
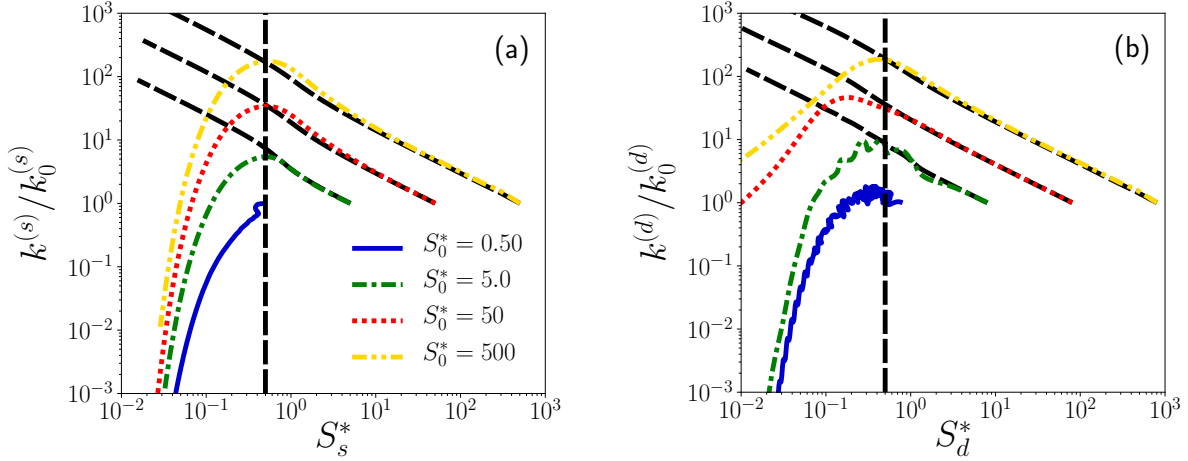

FIG. 4: (a) Solenoidal TKE against the solenoidal shear parameter $S_s^* = Sk^{(s)}/\epsilon^{(s)}$ and (b) dilatational TKE against dilatational shear parameter $S_d^* = Sk^{(d)}/\epsilon^{(d)}$. S_0^* is the initial value of the shear parameter $S^* = Sk/\epsilon$, where $S = \dot{L}/L$. $k_0^{(s)}$ and $k_0^{(d)}$ are the initial values of $k^{(s)}$ and $k^{(d)}$, respectivley. The vertical dashed line in (a) corresponds to the time at which $P^{(s)} = \langle\rho\rangle \epsilon^{(s)}$, and the vertical dashed line in (b) corresponds to the time at which $P^{(d)} = \langle\rho\rangle \epsilon^{(d)}$. The dashed diagonal lines correspond to Eq. (25).

solenoidal field. More importantly, the vertical line at which dilatational production equals dilatational dissipation no longer demarcates the domains of increasing and decreasing turbulence for all four cases, since for $S_0^* = 50$ the dilatational TKE keeps on increasing after this vertical line is reached. Lastly, Fig. 4(b) shows that the decrease in energy is slower than that observed in Fig. 4(a) for cases $S_0^* = 50$

8

and 500. This suggests that the dilatational dissipation is acting against an additional source of energy, which, as will be shown in Section IV A 2, is the pressure dilatation.

2. Budgets

Figures 5 to 8 contain the TKE budget for the solenoidal and dilatational fields. For the $S_0^* = 0.5$ case shown in Fig. 5, oscillations in the pressure dilatation and dilatational dissipation are observed. The magnitude of the oscillations in $\langle \rho \rangle \epsilon^{(d)}$ are significantly smaller than those of PD. We also note that the oscillations of the pressure dilatation and dilatational dissipation are correlated, with the dilatational dissipation slightly lagging the pressure dilatation. Moreover, the oscillations in $k^{(d)}$ shown in Fig. 3(b) are also correlated with PD, with $k^{(d)}$ lagging behind PD. This serves as evidence that pressure dilatation is responsible for the oscillatory behavior of the dilatational TKE. The strong oscillatory nature of PD has been observed elsewhere, see for example [18, 29] for the case of forced turbulence and [9, 30] for sheared turbulence. For the $S_0^* = 5.0$ case shown in Fig. 6 the oscillations in PD and $\langle \rho \rangle \epsilon^{(d)}$ have been attenuated. Figures 7 and 8 show that as the compression speed is increased to $S_0^* = 50$ and 500, PD and $\langle \rho \rangle \epsilon^{(d)}$ do not exhibit oscillations up to the last simulated instance in time.

The dashed vertical lines in Figs. 6 to 8 indicate the domain length at which the maximum value of solenoidal or dilatational TKE is achieved. As the figures show, peak values of TKE occur at larger domain lengths than peak values for sources of the TKE. An additional behavior to highlight is that for the faster compression speeds, peak values for the dilatational TKE sources occur at smaller domain lengths than those of the solenoidal energy. For example, for compression speed $S_0^* = 50$, peak values for the solenoidal dissipation and production occur at $L \approx 0.04$, whereas peak values for dilatational dissipation and pressure dilatation have not yet occurred even by the last simulated time. This same lag in peak values is observed for the $S_0^* = 500$ compression.

Figures 5 to 8 also show that the pressure dilatation is either skewed towards positive values, as is the case for $S_0^* = 0.5$, or is positive throughout the entire compression. This is further exemplified by looking at Table II, which shows the integrated values of the energy transfer mechanisms, from the initial to the last available simulated time. All integrated values for the pressure dilatation are positive.

Thus, PD behaves more as a source rather than a sink or a neutral term in the balance of dilatational TKE. As a consequence, the dilatational dissipation needs to counteract the effect of both the dilatational production and pressure dilatation for the sudden viscous dissipation to occur in the dilatational field. Given that for the two fastest compressions the integrated contribution of PD is almost as large as that of $\langle \rho \rangle \epsilon^{(d)}$, it is thus not unexpected that the dilatational TKE decays at a slower rate than the solenoidal TKE, as shown in Fig. 4.

3. Spectra

The energy spectra for the solenoidal and dilatational fields are shown in Fig. 9, for the compression speed of $S_0^* = 5.0$. The profile obtained at $L \approx 0.10$ corresponds to a time during which the sudden viscous dissipation mechanism is taking place, and the profile at $L \approx 0.04$ to a time for which most of the turbulence has already been dissipated. The shapes and trends are similar for the solenoidal and dilatational spectra. Additionally, these profiles are in qualitative agreement with results shown in [12]. As the compression proceeds, the energy in the higher modes decreases whereas the energy in the lower modes increases. The set of modes for which the energy decreases expands as the compression progresses, and eventually even the lower modes are dissipated, as shown by the profile corresponding to $L \approx 0.04$.

B. Internal energy

The temperature evolutions as a function of the domain length are shown in Fig. 10 for all the compression speeds. These are also compared against the $1/L^2$ temperature scaling corresponding to an adiabatic isentropic process with $\gamma = 5/3$, as assumed in [12]. As the figure shows, the temperature evolutions are in very close agreement with the adiabatic scaling. This indicates that the terms in the mean internal energy equation neglected under the assumption of adiabatic compression, namely the solenoidal dissipation, dilatational dissipation, and pressure dilatation, do not provide a strong contribution towards the increase of temperature for the current simulations.

The negligible effect of the dissipations and the pressure dilatation is confirmed by comparing the source terms of the mean internal energy, as is done
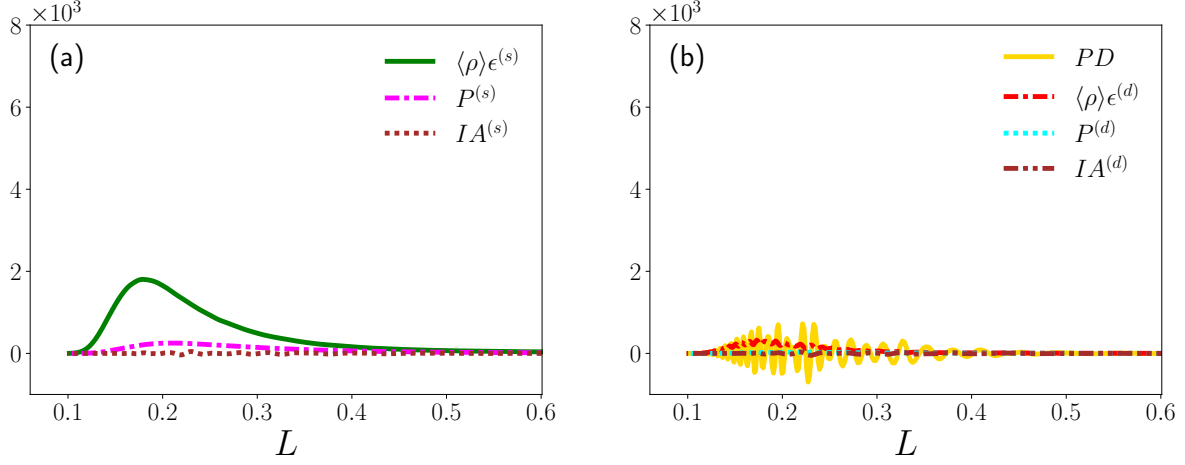
9

FIG. 5: TKE budget for the (a) solenoidal and (b) dilatational flow fields, given $S_0^* = 0.5$. The initial length of the domain is $L = 1$, which decreases as time progresses. All terms have been normalized by $\rho_0 U_0^3 / L_0$.
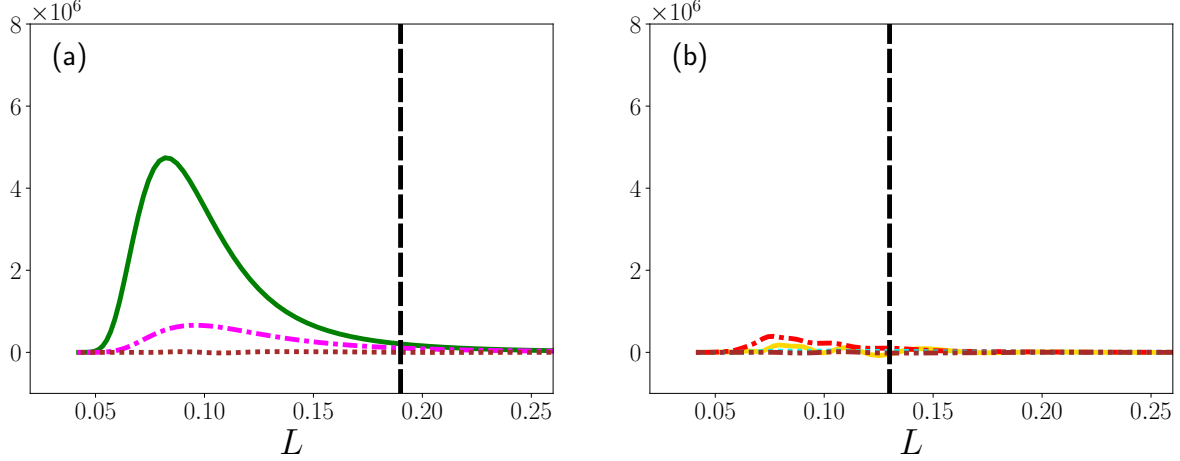

FIG. 6: TKE budget for the (a) solenoidal and (b) dilatational flow fields, given $S_0^* = 5.0$. The initial length of the domain is $L = 1$, which decreases as time progresses. All terms have been normalized by $\rho_0 U_0^3 / L_0$. The same legend as that of Fig. 5 applies to the plots above. The vertical dashed line corresponds to the domain size at which peak solenoidal TKE (a) and peak dilatational TKE (b) are achieved.

in Fig. 11. These figures show that, throughout the compression, the dominant source in the mean internal-energy equation is the mechanical work, which takes the form of $MW = -3\langle P \rangle \dot{L}/L$ for the given isotropic compression of Eq. (4). For all compression speeds tested, the solenoidal dissipation, dilatational dissipation, and pressure dilatation are eclipsed by the mechanical work at all times during the compression. However, for the two fastest compression rates, the peak values of the dilatational dissipation and pressure dilatation are not achieved by the last-available simulated instance in time. Nonetheless, as shown in Fig. 3, by this last simulated instance in time the dilatational TKE
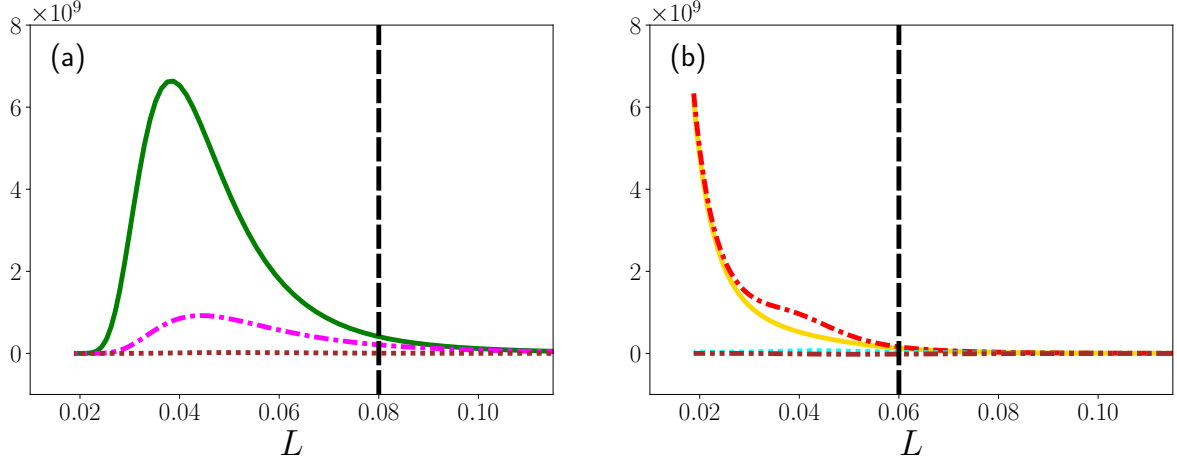
10

FIG. 7: TKE budget for the (a) solenoidal and (b) dilatational flow fields, given $S_0^* = 50$. The initial length of the domain is $L = 1$, which decreases as time progresses. All terms have been normalized by $\rho_0 U_0^3/L_0$. The same legend as that of Fig. 5 applies to the plots above. The vertical dashed line corresponds to the domain size at which peak solenoidal TKE (a) and peak dilatational TKE (b) are achieved.
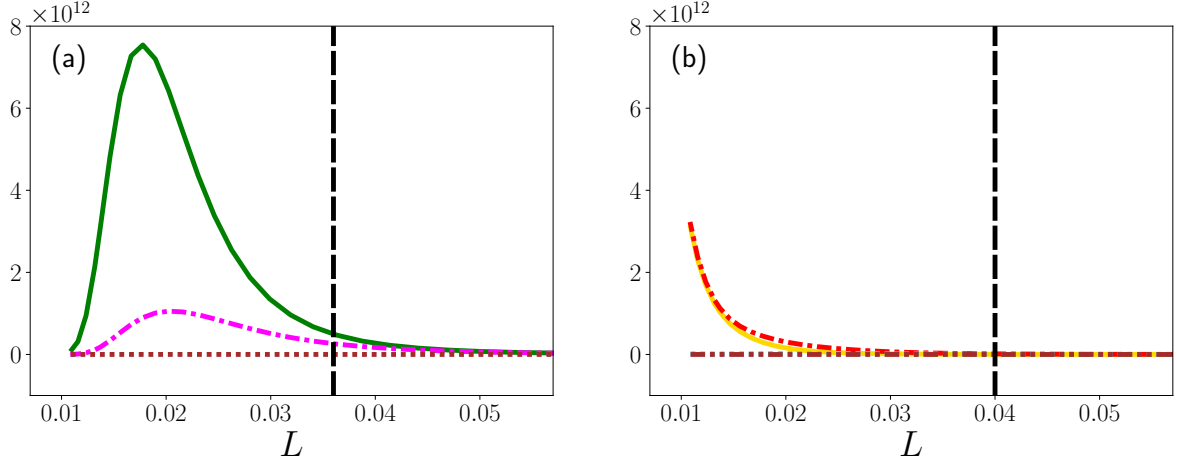

FIG. 8: TKE budget for the (a) solenoidal and (b) dilatational flow fields, given $S_0^* = 500$. The initial length of the domain is $L = 1$, which decreases as time progresses. All terms have been normalized by $\rho_0 U_0^3/L_0$. The same legend as that of Fig. 5 applies to the plots above. The vertical dashed line corresponds to the domain size at which peak solenoidal TKE (a) and peak dilatational TKE (b) are achieved.

has already surpassed its peak value and has dissipated by more than an order of magnitude, and it is thus unlikely that the dilatational dissipation and pressure dilatation will ever overtake the mechanical work. Since the mechanical work overpowers the other sources of mean internal energy, the simulation results should follow the idealized adiabatic compression scalings. For the specific-heat ratio of $\gamma = 5/3$ and the assumption of an adiabatic compression, the mechanical work scales as $1/L^6$, which

11

TABLE II: Integrated energy sources given different compression speeds. All values are normalized by $\rho_0 U_0^2$.

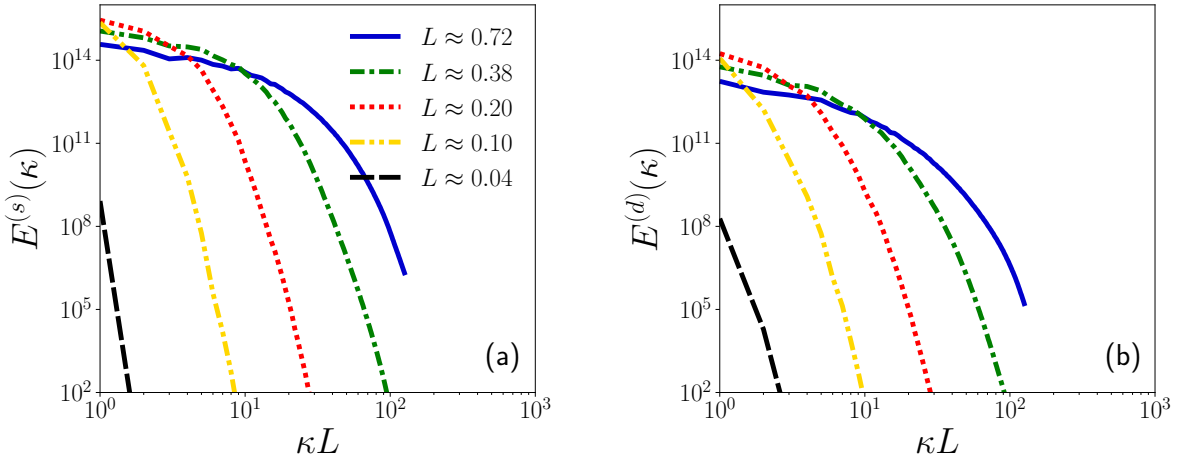|	$S_0^* = 0.5$	$S_0^* = 5.0$	$S_0^* = 50$	$S_0^* = 500$
$IA^{(s)}$	2.32×10^{-1}	4.80×10^{1}	4.45×10^{3}	4.90×10^{3}
$IA^{(d)}$	-2.32×10^{-1}	-4.80×10^{1}	-4.45×10^{3}	-4.90×10^{3}
$P^{(s)}$	2.89×10^{1}	3.08×10^{3}	1.97×10^{5}	1.03×10^{7}
$P^{(d)}$	2.80×10^{0}	1.57×10^{2}	1.39×10^{4}	3.23×10^{5}
$\langle\rho\rangle\,\epsilon^{(s)}$	1.46×10^{2}	1.54×10^{4}	9.82×10^{5}	5.07×10^{7}
$\langle\rho\rangle\,\epsilon^{(d)}$	1.87×10^{1}	1.07×10^{3}	3.24×10^{5}	6.59×10^{6}
PD	4.89×10^{0}	3.34×10^{2}	2.64×10^{5}	5.15×10^{6}
MW	3.34×10^{5}	2.69×10^{7}	1.35×10^{9}	2.14×10^{10}

FIG. 9: Energy spectra for the (a) solenoidal and (b) dilatational TKE, at different times (or domain lengths) throughout the compression. The spectra correspond to the $S_0^* = 5.0$ case.

is shown as black dots in Fig. 11. As expected, this is in close agreement with the actual mechanical work, given by the blue dashed-double-dotted lines. The minor difference between the blue lines and the black dots is due to the fact that the terms neglected in an idealized adiabatic compression, such as the viscous dissipation, thermal conduction, and pressure dilatation, are not identically zero in the Miranda code.

The dominance of the mechanical work can be further exemplified by considering the integrated values of the mean internal energy sources, shown in Table II. The time-integrated contribution towards the increase of temperature due to mechanical work is at least three orders of magnitude larger than the second most significant time-integrated source term,

namely, the solenoidal dissipation. A similar metric for highlighting the dominance of the mechanical work is the comparison of the time-integrated total contribution from the TKEs to mean internal energy against the time-integrated total contribution from the mean kinetic energy to the mean internal energy. The ratio of these two factors for the four cases $S_0^* = 0.50, 5.0, 50,$ and, 500 is 0.0005, 0.0006, 0.0008, and 0.002, respectively.

Given that, for the parameters used in these simulations, the dissipated turbulent kinetic energy does not significantly increase the temperature of the system above the adiabatic prediction, it is crucial to determine under which conditions would the dissipated TKE actually lead to meaningful increases in
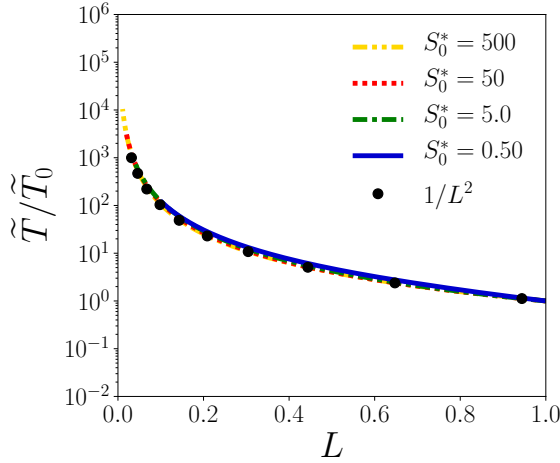
FIG. 10: Evolution of temperature as a function of the size of the domain. The initial temperature is denoted by $\widetilde{T}_0$.

temperature. To do this, we make use of the relation

$$\frac{d}{dt}\left(\frac{\widetilde{U}+k}{\widetilde{U}^{(a)}}\right) = 0, \quad (26)$$

which is derived in Appendix B. $\widetilde{U}^{(a)}$ is the mean internal energy of the system given the idealized adiabatic compression, and is thus given by $\widetilde{U}^{(a)} = \widetilde{U}_0 L^{-2}$, where $\widetilde{U}_0$ is the initial value of $\widetilde{U}$. Integrating from the initial time t_0 to a final time t_f, one obtains

$$\left.\frac{\widetilde{U}+k}{\widetilde{U}^{(a)}}\right|_{t_f} = \left.\frac{\widetilde{U}+k}{\widetilde{U}^{(a)}}\right|_{t_0} = 1 + \frac{k_0}{\widetilde{U}_0} = 1 + \frac{5}{9}M_{u,0}^2. \quad (27)$$

In the above we have made use of the definition of the fluctuating Mach number [9]

$$M_u = \frac{\sqrt{\widetilde{u_i'' u_i''}}}{c(\widetilde{T})}, \quad (28)$$

whose initial value is denoted by $M_{u,0}$. We introduce $\widetilde{T}^{(a)} = \widetilde{T}_0 L^{-2}$ as the temperature corresponding to an adiabatic compression. If we define t_f as the time by which all of the turbulent kinetic energy has dissipated, and $\widetilde{T}_f$ and $\widetilde{T}_f^{(a)}$ as the temperatures $\widetilde{T}$ and $\widetilde{T}^{(a)}$ at times $t > t_f$, respectively, then Eq. (27) can be expressed as

$$\frac{\widetilde{T}_f}{\widetilde{T}_f^{(a)}} = 1 + \frac{5}{9}M_{u,0}^2. \quad (29)$$

The above relation highlights a few notable aspects of the compression mechanism. Given $\widetilde{T}_0$ and k_0, $M_{u,0}$ is known, which, along with values of L smaller than those corresponding to the time t_f, can be used in Eq. (29) to obtain the temperature after the TKE has been fully dissipated. The second aspect to highlight is that the temperature ratio $\widetilde{T}_f/\widetilde{T}_f^{(a)}$ is independent of the compression speed. Thus, whether the system is compressed slowly so that there is no sudden viscous dissipation or the compression is rapid and thus the sudden viscous dissipation occurs, the temperature obtained after all the TKE has been depleted will always be of the same proportion to the idealized adiabatic temperature.

For the simulations described in this paper, the initial fluctuating Mach number immediately preceding the start of the compression is $M_{u,0} = 0.651$. Using Eq. (29), this gives $\widetilde{T}_f/\widetilde{T}_f^{(a)} = 1.235$. Table III lists this ratio computed from simulation data available at the last simulated instance in time, for the four compression speeds. As the table shows, there is strong agreement with the analytical value of 1.235. The slightly lower ratio for the fastest compression is most likely due to the fact that all of the TKE, specially the dilatational TKE, has not yet fully dissipated into heat. Equation (29) can now thus be used to predict under which conditions the dissipated TKE would lead to meaningful increases in temperature. For subsonic initial fluctuating Mach numbers, the temperature post TKE depletion can be up to about 1.5 times larger than that obtained with an adiabatic compression. If supersonic Mach numbers are used, such as $M_{u,0} = 2$ and 5, then the temperature post TKE depletion would be about 3 and 15 times larger, respectively, than for an adiabatic compression. For highly supersonic turbulence such as that encountered in the interstellar medium [31, 32], a Mach number of $M_{u,0} = 17$ would lead to final temperatures about 160 times higher than those predicted assuming an adiabatic scaling. As stated in [16], the hot spot of an ICF capsule can be characterized by a turbulent Mach number $M_t \approx 0.4$. Using this value in Eq. (29) leads to $\widetilde{T}_f/\widetilde{T}_f^{(a)} \approx 1.09$. This increase of temperature is minimal, and is eclipsed by the effect of the mechanical work. For example, if we assume that the sudden viscous dissipation of TKE occurs at $L = 0.1$, a small reduction of the domain size to $L = 0.0958$ would already allow the mechanical work to generate an equivalent increase in temperature. It is thus expected that only for flow fields with large initial Mach numbers would the self-consistent feedback mechanism lead to sudden dissipations with significant effects.
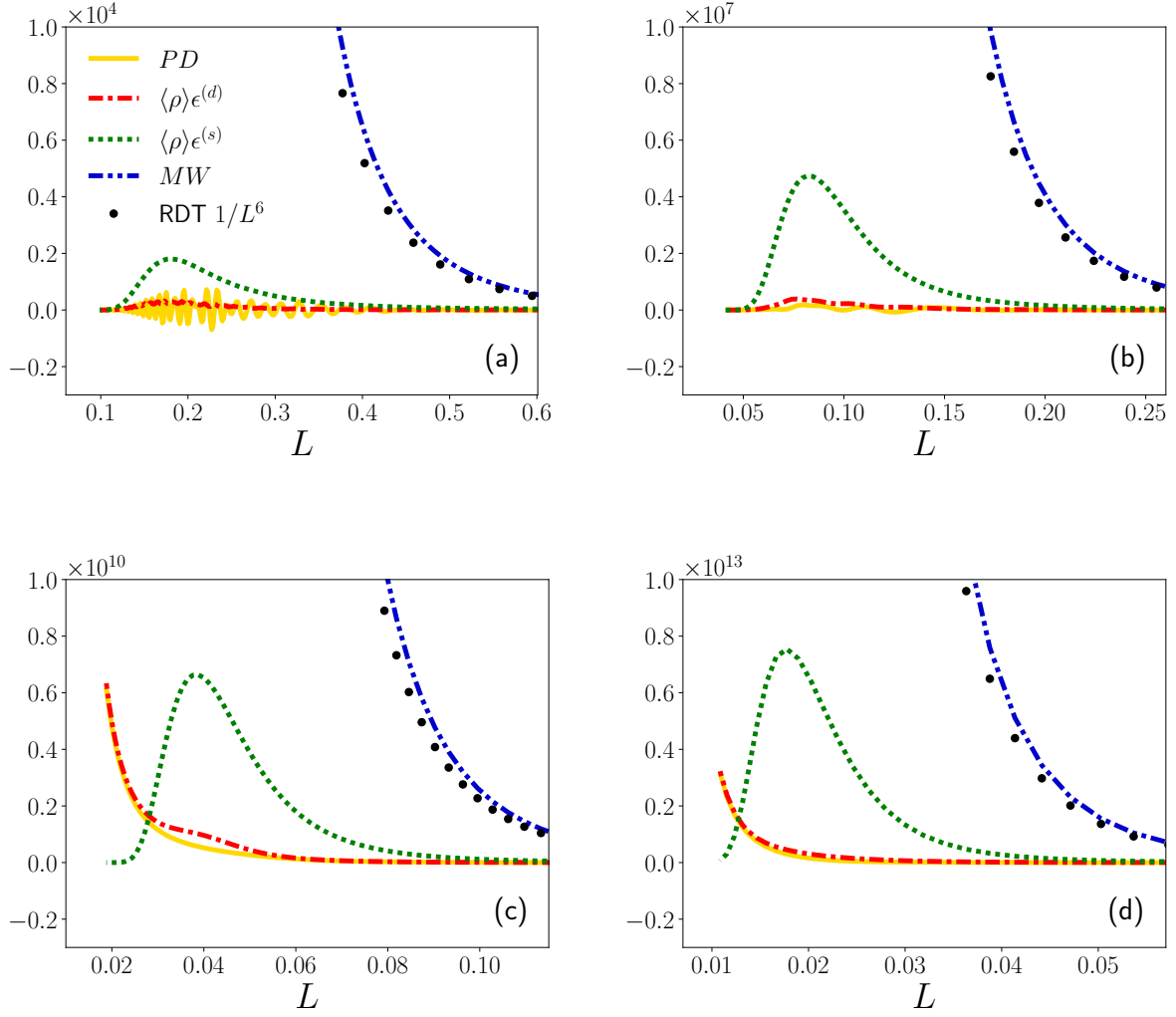
13

FIG. 11: Mean internal energy budget for the four compression speeds (a) $S^* = 0.5$, (b) $S^* = 5.0$, (c) $S^* = 50$, and (d) $S^* = 500$. The initial length of the domain is $L = 1$, which decreases as time progresses. All terms have been normalized by $\rho_0 U_0^3 / L_0$.

TABLE III: Ratio $\widetilde{T}_f / \widetilde{T}_f^{(a)}$ obtained at the last simulated instance in time.

	$S_0^* = 0.50$	$S_0^* = 5.0$	$S_0^* = 50$	$S_0^* = 500$
$\dfrac{\widetilde{T}_f}{\widetilde{T}_f^{(a)}}$	1.232	1.232	1.232	1.230

V. CONCLUDING REMARKS

A sudden viscous dissipation of plasma turbulence under compression was demonstrated in [12]. We expand on this previous work by accounting for the self-consistent feedback loop associated with this viscous mechanism. The feedback loop entails a transfer of energy from the turbulence towards the internal energy, and the subsequent increased temperatures and viscosities that in turn accelerate the original dissipation of TKE. Although previous efforts

have reproduced the sudden dissipation of TKE, these do not capture the subsequent effect of the dissipated energy on the temperature, and the consequences thereof. This limitation is due to the use of the zero-Mach-limit assumption. To capture the increase of internal energy resulting from the dissipated TKE, and thus account for the entire self-consistent feedback loop, direct numerical simulations have been carried out using a finite-Mach number formulation that solves transport equations for the density, fluctuating velocity, and total energy. The analysis of the self-consistent feedback loop was divided into two parts: the first focused on the evolution of the solenoidal and dilatational TKEs, and the second on the evolution of the mean internal energy as it absorbs the dissipated TKE.

The first part of the analysis revealed new insights into finite-Mach-number flow physics for this particular compression. The simulations show that not only the solenoidal but also the dilatational TKE experiences the sudden viscous dissipation. Although this outcome might initially seem expected, it is instead a somewhat subtle result given that the time-integrated effect of the pressure dilatation is to transfer energy from heat towards dilatational TKE, even for cases when the pressure dilatation transfers energy in both directions on short time scales. Thus, the dilatational dissipation has had to counteract both the dilatational production and pressure dilatation for the sudden viscous dissipation of dilatational TKE to take place. The simulations also showed that both the solenoidal and dilatational modes do not evolve in synchrony, since, for the largest compression speeds, peaks in the sources for dilatational TKE occur well after those of the solenoidal TKE. Finally, large oscillations in the temporal evolution of dilatational TKE for slow compression rates are observed, which are correlated with the highly-oscillatory nature of the pressure dilatation.

The second part of the analysis revealed that mechanical work, which transforms energy from the mean flow to increase heat, dominates all other sources of mean internal energy for the turbulent Mach numbers chosen in this study. For all instances in time, the mechanical work term is larger, often by multiple orders of magnitude, than the solenoidal and dilatational dissipation and the pressure dilatation. As a result, the contribution of the dissipated TKE towards the increase of temperature is minimal, and the temperature evolution closely follows an adiabatic scaling. This validates previous efforts [12–15] that relied on a fixed adiabatic scaling for the temperature evolution.

So as to estimate for which parameters the suddenly-dissipated TKE would lead to a significant increase in temperature, a simple analytical expression was derived for the ratio of the temperature post TKE depletion to the idealized adiabatic temperature. This ratio depends on the initial fluctuating Mach number only, indicating that the rate of compression does not affect the magnitudes of the temperature post TKE depletion. The derived analytical expression confirms that for subsonic initial fluctuating Mach numbers the true temperature of the system can not be substantially larger than the adiabatic temperature. To provide a point of reference, it was shown that all of the suddenly-dissipated TKE for an initial turbulent Mach number characteristic of an ICF implosion would have an equivalent effect as that of an adiabatic compression from $L = 0.1$ to only $L = 0.0958$. Scenarios where the the turbulence is highly supersonic are thus required for the dissipated TKE to have a significant contribution. It is still a matter of debate whether hydrodynamic instabilities develop into turbulence during a short-lived ICF implosion [4, 33, 34], let alone a transition to significant turbulence intensities characteristic of supersonic turbulence. Thus, the potential of the sudden viscous dissipation mechanism to significantly enhance the heating of the plasma by dissipating the inherent turbulence could be limited for this application. Nonetheless, this viscous mechanism could serve as an effective tool to diminish detrimental turbulent mixing if hydrodynamic instabilities do transition into a turbulent state. It is also crucial to highlight that the finite-Mach-number framework chosen here, although more general than the zero-Mach-number formalism, is still missing physics relevant to ICF, such as non-ideal equations of state, radiation transport, multiple species, plasma viscosity models, separate ion and electron temperatures, alpha heating, and non-isotropic compressions, which could all affect the conclusions reached herein. Thus, these factors need to be explored to provide a definite assessment on the ability of the sudden viscous dissipation mechanism to improve the performance of ICF.

Appendix A: Derivation of the finite-Mach-number Navier-Stokes equations for isotropic mean compression

The derivation of the governing equations used for the computational simulations in this study is detailed below. This derivation is divided into five distinct steps, each described in the five subsections below.

1. Compressible Navier-Stokes equations

The starting point are the Navier-Stokes equations for a compressible fluid. Thus, the evolution of the density $\rho = \rho(t, \mathbf{x})$, velocity $U_i = U_i(t, \mathbf{x})$ and total energy $E = E(t, \mathbf{x})$ is governed by

$$\frac{\partial \rho}{\partial t} + \frac{\partial \rho U_i}{\partial x_i} = 0, \tag{A1}$$

$$\frac{\partial \rho U_i}{\partial t} + \frac{\partial \rho U_i U_j}{\partial x_j} = \frac{\partial \sigma_{ij}}{\partial x_j}, \tag{A2}$$

$$\frac{\partial \rho E}{\partial t} + \frac{\partial \rho E U_j}{\partial x_j} = \frac{\partial U_i \sigma_{ij}}{\partial x_j} + \frac{\partial}{\partial x_j}\left(\kappa \frac{\partial T}{\partial x_j}\right). \tag{A3}$$

Closure of the above is achieved with

$$\sigma_{ij} = -P\delta_{ij} + 2\mu\left[\frac{1}{2}\left(\frac{\partial U_i}{\partial x_j} + \frac{\partial U_j}{\partial x_i}\right) - \frac{1}{3}\frac{\partial U_k}{\partial x_k}\delta_{ij}\right], \tag{A4}$$

$$E = U + K, \tag{A5}$$

$$U = C_v T \qquad K = \frac{1}{2}U_i U_i, \tag{A6}$$

$$P = \rho R T, \tag{A7}$$

$$\kappa = \frac{\mu C_p}{Pr}, \tag{A8}$$

$$\mu = \mu_0 \left(\frac{T}{T_0}\right)^n. \tag{A9}$$

$P = P(t, \mathbf{x})$ is the pressure, $T = T(t, \mathbf{x})$ the temperature, $U = U(t, \mathbf{x})$ the internal energy, $K = K(t, \mathbf{x})$ the kinetic energy, $\mu = \mu(t, \mathbf{x})$ the dynamic viscosity, and $\kappa = \kappa(t, \mathbf{x})$ the thermal conductivity. C_v, C_p, R, and Pr are the specific heat at constant volume, the specific heat at constant pressure, the ideal gas constant, and the Prandtl number, respectively. For the power law of viscosity, μ_0 and T_0 represent reference viscosity and temperature values, and n is the power-law exponent.

2. Homogeneous turbulence

We summarize here and in the following subsection the derivations carried out by [9] to obtain the governing equations for homogeneous compressible turbulence. The quantities $\langle \rho \rangle$ and $\langle P \rangle$ are defined as Reynolds-averaged density and pressure, respectively, and $\widetilde{U}_i$ as the Favre-averaged velocity. [9] showed that for turbulence to remain homogeneous, necessary and sufficient conditions are that $\langle \rho \rangle$ and $\langle P \rangle$ depend on t but not $\mathbf{x}$, and that $\tilde{U}_i$ be given by

$$\tilde{U}_i = G_{ij} x_j, \tag{A10}$$

where $G_{ij} = \frac{\partial \tilde{U}_i}{\partial x_j}$ also depends only on t and not $\mathbf{x}$. Given the above assumptions, averaging of the momentum equation shows that the evolution of G_{ij} is dictated by

$$\frac{dG_{ij}}{dt} + G_{kj}G_{ik} = 0. \tag{A11}$$

Moreover, using the assumptions above and plugging in the decomposition $U_i = \widetilde{U}_i + u_i''$ in Eqs. (A1) to (A4), [9] derived the governing equations in terms of the fluctuating velocity. These are

$$\frac{\partial \rho}{\partial t} + \frac{\partial \rho}{\partial x_i}G_{ij}x_j + \frac{\partial \rho u_i''}{\partial x_i} = f^{(\rho)}, \tag{A12}$$

$$\frac{\partial \rho u_i''}{\partial t} + \frac{\partial \rho u_i''}{\partial x_j}G_{jk}x_k + \frac{\partial \rho u_i'' u_j''}{\partial x_j} = \frac{\partial \sigma_{ij}}{\partial x_j} + f_i^{(u)}, \tag{A13}$$

$$\frac{\partial \rho E_t}{\partial t} + \frac{\partial \rho E_t}{\partial x_i}G_{ik}x_k + \frac{\partial \rho E_t u_i''}{\partial x_i} =$$
$$\frac{\partial u_i'' \sigma_{ij}}{\partial x_j} + \frac{\partial}{\partial x_j}\left(\kappa \frac{\partial T}{\partial x_j}\right) + f^{(e)}. \tag{A14}$$

Closure of the above is achieved with

$$\sigma_{ij} = -P\delta_{ij} +$$
$$2\mu\left[\frac{1}{2}\left(\frac{\partial u_i''}{\partial x_j} + \frac{\partial u_j''}{\partial x_i}\right) - \frac{1}{3}\frac{\partial u_k''}{\partial x_k}\delta_{ij}\right] +$$
$$2\mu\left[\frac{1}{2}\left(G_{ij} + G_{ji}\right) - \frac{1}{3}G_{ii}\delta_{ij}\right], \tag{A15}$$

$$E_t = U + K_t, \tag{A16}$$

$$U = C_v T \qquad K_t = \frac{1}{2}u_i'' u_i'', \tag{A17}$$

$$P = \rho R T, \tag{A18}$$

$$\kappa = \frac{\mu C_p}{Pr}, \tag{A19}$$

$$\mu = \mu_0 \left(\frac{T}{T_0}\right)^n, \tag{A20}$$

$$f^{(\rho)} = -\rho G_{ii}, \tag{A21}$$

$$f_i^{(u)} = -\rho u_j'' G_{ij} - \rho u_i'' G_{jj}, \tag{A22}$$

$$f^{(e)} = -\rho E_t G_{ii} - \rho u_i'' u_j'' G_{ij} + G_{ij}\sigma_{ij}. \tag{A23}$$

3. Rogallo transformation

As is typically done for simulations of homogeneous turbulence (see for example [9, 35]) one can reformulate the equations using a deforming reference frame—referred to here as the Rogallo reference frame—to eliminate those terms in Eqs. (A12) to (A14) that have an explicit dependence on position. The variables in the Rogallo reference frame are denoted as $\mathring{\rho} = \mathring{\rho}(t, \mathring{\mathbf{x}})$, $\mathring{u}'' = \mathring{u}''(t, \mathring{\mathbf{x}})$, $\mathring{P} = \mathring{P}(t, \mathring{\mathbf{x}})$, $\mathring{T} = \mathring{T}(t, \mathring{\mathbf{x}})$. The relationship between the variables in the original reference frame and the Rogallo reference frame is

$$\begin{aligned}
\rho &= \mathring{\rho}(t, \mathbf{f}) \\
u_i'' &= \mathring{u}_i''(t, \mathbf{f}) \\
P &= \mathring{P}(t, \mathbf{f}) \\
T &= \mathring{T}(t, \mathbf{f}),
\end{aligned} \tag{A24}$$

where $f_i = A_{ij} x_j$. A_{ij} is referred to as the coordinate-transformation tensor, it depends on t only, and is defined so as to satisfy

$$\frac{dA_{ij}}{dt} + A_{ik} G_{kj} = 0. \tag{A25}$$

Using this transformation, the governing equations in the Rogallo reference frame are

$$\frac{\partial \mathring{\rho}}{\partial t} + \frac{\partial \mathring{\rho} \mathring{u}_i''}{\partial \mathring{x}_j} A_{ji} = \mathring{f}^{(\rho)}, \tag{A26}$$

$$\frac{\partial \mathring{\rho} \mathring{u}_i''}{\partial t} + \frac{\partial \mathring{\rho} \mathring{u}_i'' \mathring{u}_j''}{\partial \mathring{x}_k} A_{kj} = \frac{\partial \mathring{\sigma}_{ij}}{\partial \mathring{x}_k} A_{kj} + \mathring{f}_i^{(u)}, \tag{A27}$$

$$\frac{\partial \mathring{\rho} \mathring{E}_t}{\partial t} + \frac{\partial \mathring{\rho} \mathring{E}_t \mathring{u}_i''}{\partial \mathring{x}_j} A_{ji} =$$
$$\frac{\partial \mathring{u}_i'' \mathring{\sigma}_{ij}}{\partial \mathring{x}_k} A_{kj} + \frac{\partial}{\partial \mathring{x}_l} \left(\mathring{\kappa} \frac{\partial \mathring{T}}{\partial \mathring{x}_k}\right) A_{kj} A_{lj} + \mathring{f}^{(e)}. \tag{A28}$$

Closure of the above is achieved with

$$\mathring{\sigma}_{ij} = -\mathring{P}\delta_{ij} +$$
$$2\mathring{\mu}\left[\frac{1}{2}\left(\frac{\partial \mathring{u}_i''}{\partial \mathring{x}_n} A_{nj} + \frac{\partial \mathring{u}_j''}{\partial \mathring{x}_n} A_{ni}\right) - \frac{1}{3}\frac{\partial \mathring{u}_k''}{\partial \mathring{x}_n} A_{nk}\delta_{ij}\right] +$$
$$2\mathring{\mu}\left[+\frac{1}{2}\left(G_{ij} + G_{ji}\right) - \frac{1}{3}G_{ii}\delta_{ij}\right], \tag{A29}$$

$$\mathring{E}_t = \mathring{U} + \mathring{K}_t, \tag{A30}$$

$$\mathring{U} = C_v \mathring{T} \qquad \mathring{K}_t = \frac{1}{2}\mathring{u}_i''\mathring{u}_i'', \tag{A31}$$

$$\mathring{P} = \mathring{\rho} R \mathring{T}, \tag{A32}$$

$$\mathring{\kappa} = \frac{\mathring{\mu} C_p}{Pr}, \tag{A33}$$

$$\mathring{\mu} = \mu_0 \left(\frac{\mathring{T}}{T_0}\right)^n, \tag{A34}$$

$$\mathring{f}^{(\rho)} = -\mathring{\rho} G_{ii}, \tag{A35}$$

$$\mathring{f}_i^{(u)} = -\mathring{\rho}\mathring{u}_j'' G_{ij} - \mathring{\rho}\mathring{u}_i'' G_{jj}, \tag{A36}$$

$$\mathring{f}^{(e)} = -\mathring{\rho}\mathring{E}_t G_{ii} - \mathring{\rho}\mathring{u}_i''\mathring{u}_j'' G_{ij} + G_{ij}\mathring{\sigma}_{ij}. \tag{A37}$$

4. Isotropic compression

The mean flow deformation for isotropic compression is given in [7, 9, 12], and can be expressed as

$$G_{ij} = \frac{\dot{L}}{L}\delta_{ij}, \tag{A38}$$

where $\dot{L}$ is constant and thus $L = 1 + \dot{L}t$. The corresponding coordinate transformation tensor is

$$A_{ij} = \frac{1}{L}\delta_{ij}. \tag{A39}$$

Thus, using the above in Eqs. (A26) to (A28), we obtain

$$\frac{\partial \mathring{\rho}}{\partial t} + \frac{\partial \mathring{\rho}\mathring{u}_i''}{\partial \mathring{x}_i}\frac{1}{L} = \mathring{f}^{(\rho)}, \tag{A40}$$

$$\frac{\partial \mathring{\rho}\mathring{u}_i''}{\partial t} + \frac{\partial \mathring{\rho}\mathring{u}_i''\mathring{u}_j''}{\partial \mathring{x}_j}\frac{1}{L} = \frac{\partial \mathring{\sigma}_{ij}}{\partial \mathring{x}_j}\frac{1}{L} + \mathring{f}_i^{(u)}, \tag{A41}$$

$$\frac{\partial \mathring{\rho}\mathring{E}_t}{\partial t} + \frac{\partial \mathring{\rho}\mathring{E}_t\mathring{u}_i''}{\partial \mathring{x}_i}\frac{1}{L} =$$
$$\frac{\partial \mathring{u}_i''\mathring{\sigma}_{ij}}{\partial \mathring{x}_j}\frac{1}{L} + \frac{\partial}{\partial \mathring{x}_j}\left(\mathring{\kappa}\frac{\partial \mathring{T}}{\partial \mathring{x}_j}\right)\frac{1}{L^2} + \mathring{f}^{(e)}. \tag{A42}$$

Closure of the above is achieved with

$$\mathring{\sigma}_{ij} = -\mathring{P}\delta_{ij} +$$
$$2\mathring{\mu}\left[\frac{1}{2}\left(\frac{\partial \mathring{u}_i''}{\partial \mathring{x}_j}\frac{1}{L} + \frac{\partial \mathring{u}_j''}{\partial \mathring{x}_i}\frac{1}{L}\right) - \frac{1}{3}\frac{\partial \mathring{u}_k''}{\partial \mathring{x}_k}\frac{1}{L}\delta_{ij}\right], \tag{A43}$$

$$\mathring{E}_t = \mathring{U} + \mathring{K}_t, \tag{A44}$$

$$\mathring{U} = C_v\mathring{T} \qquad \mathring{K}_t = \frac{1}{2}\mathring{u}_i''\mathring{u}_i'', \tag{A45}$$

$$\mathring{P} = \mathring{\rho}R\mathring{T}, \tag{A46}$$

$$\mathring{\kappa} = \frac{\mathring{\mu}C_p}{Pr}, \tag{A47}$$

$$\mu = \mu_0\left(\frac{\mathring{T}}{T_0}\right)^n, \tag{A48}$$

$$\mathring{f}^{(\rho)} = -3\mathring{\rho}\frac{\dot{L}}{L}, \tag{A49}$$

$$\mathring{f}_i^{(u)} = -4\mathring{\rho}\mathring{u}_i''\frac{\dot{L}}{L}, \tag{A50}$$

$$\mathring{f}^{(e)} = -3\mathring{\rho}\mathring{E}_t\frac{\dot{L}}{L} - \mathring{\rho}\mathring{u}_i''\mathring{u}_i''\frac{\dot{L}}{L} - 3\mathring{P}\frac{\dot{L}}{L}. \tag{A51}$$

5. Re-scaling

An additional transformation can be performed so that, as the simulation advances in time, division by very small values of L is avoided. The analogue of this re-scaling for the zero-Mach limit is detailed in [12] and in the Appendix of [13]. The new re-scaled flow variables are $\hat{\rho} = \hat{\rho}(\hat{t}, \mathring{\mathbf{x}})$, $\hat{u}_i'' = \hat{u}_i''(\hat{t}, \mathring{\mathbf{x}})$, $\hat{P} = \hat{P}(\hat{t}, \mathring{\mathbf{x}})$, and $\hat{T} = \hat{T}(\hat{t}, \mathring{\mathbf{x}})$. Their relation to the original variables is

$$\mathring{\rho} = \hat{\rho}(g, \mathring{\mathbf{x}})L^{-1}$$
$$\mathring{u}_i'' = \hat{u}_i''(g, \mathring{\mathbf{x}})$$
$$\mathring{P} = \hat{P}(g, \mathring{\mathbf{x}})L^{-1}$$
$$\mathring{T} = \hat{T}(g, \mathring{\mathbf{x}}), \tag{A52}$$

where $g = g(t)$ is defined by $\frac{dg}{dt} = L^{-1}$.

Using this re-scaling, the governing equations become

$$\frac{\partial \hat{\rho}}{\partial \hat{t}} + \frac{\partial \hat{\rho}\hat{u}_i''}{\partial \mathring{x}_i} = \hat{f}^{(\rho)}, \tag{A53}$$

$$\frac{\partial \hat{\rho}\hat{u}_i''}{\partial \hat{t}} + \frac{\partial \hat{\rho}\hat{u}_i''\hat{u}_j''}{\partial \mathring{x}_j} = \frac{\partial \hat{\sigma}_{ij}}{\partial \mathring{x}_j} + \hat{f}_i^{(u)}, \tag{A54}$$

$$\frac{\partial \hat{\rho}\hat{E}_t}{\partial \hat{t}} + \frac{\partial \hat{\rho}\hat{E}_t\hat{u}_i''}{\partial \mathring{x}_i} = \frac{\partial \hat{u}_i''\hat{\sigma}_{ij}}{\partial \mathring{x}_j} + \frac{\partial}{\partial \mathring{x}_j}\left(\hat{\kappa}\frac{\partial \hat{T}}{\partial \mathring{x}_j}\right) + \hat{f}^{(e)}. \tag{A55}$$

Closure of the above is achieved with

$$\hat{\sigma}_{ij} = -\hat{P}\delta_{ij} + 2\hat{\mu}\left[\frac{1}{2}\left(\frac{\partial \hat{u}_i''}{\partial \mathring{x}_j} + \frac{\partial \hat{u}_j''}{\partial \mathring{x}_i}\right) - \frac{1}{3}\frac{\partial \hat{u}_k''}{\partial \mathring{x}_k}\delta_{ij}\right], \tag{A56}$$

$$\hat{E}_t = \hat{U} + \hat{K}_t, \tag{A57}$$

$$\hat{U} = C_v\hat{T} \qquad \hat{K}_t = \frac{1}{2}\hat{u}_i''\hat{u}_i'', \tag{A58}$$

$$\hat{P} = \hat{\rho}R\hat{T}, \tag{A59}$$

$$\hat{\kappa} = \frac{\hat{\mu}C_p}{Pr}, \tag{A60}$$

$$\hat{\mu} = \mu_0\left(\frac{\hat{T}}{T_0}\right)^n, \tag{A61}$$

$$\hat{f}^{(\rho)} = -2\dot{L}\hat{\rho}, \qquad (A62)$$

$$\hat{f}_i^{(u)} = -3\dot{L}\hat{\rho}\hat{u}_i'', \qquad (A63)$$

$$\hat{f}^{(e)} = -\left[2\hat{\rho}\hat{E}_t + \hat{\rho}\hat{u}_i''\hat{u}_i'' + 3\hat{P}\right]\dot{L}. \qquad (A64)$$

The last issue to be addressed is the time $\hat{t}$ that corresponds to $L = 0$. Solving $\frac{dg}{dt} = L^{-1}$ leads to

$$g = -\frac{1}{2V_b}\ln(L). \qquad (A65)$$

Since we evaluated the equations at time $t = g^{-1}(\hat{t})$, we have

$$\hat{t} = -\frac{1}{2V_b}\ln(L). \qquad (A66)$$

Thus, $L = 0$ corresponds to $\hat{t} \to \infty$. However, it is not expected that the simulation will need to proceed up to infinity, and that instead the viscous instability would kick in prior to this limit.

Appendix B: Proof of time invariance for the energy ratio $\left(\widetilde{U} + k\right)/\widetilde{U}^{(a)}$

The chain rule applied to the time derivative of the energy ratio gives

$$\frac{d}{dt}\left(\frac{\widetilde{U} + k}{\widetilde{U}^{(a)}}\right) =$$
$$\frac{d}{dt}\left(\widetilde{U} + k\right)\frac{1}{\widetilde{U}^{(a)}} + \left(\widetilde{U} + k\right)\frac{d}{dt}\left(\frac{1}{\widetilde{U}^{(a)}}\right). \quad (B1)$$

Given the definition of the adiabatic internal energy $\widetilde{U}^{(a)} = \widetilde{U}_0 L^{-2}$, we have

$$\frac{d}{dt}\left(\frac{1}{\widetilde{U}^{(a)}}\right) = \frac{2L\dot{L}}{\widetilde{U}_0}. \qquad (B2)$$

Using Eqs. (16), (17) and (19), one obtains

$$\frac{d}{dt}\left(\widetilde{U} + k\right) = \frac{MW + P}{\langle\rho\rangle}, \qquad (B3)$$

where P is the total production $P^{(s)} + P^{(d)}$. Given the deformation tensor G_{ij} used for isotropic compressions, $MW = -3\langle P\rangle\dot{L}/L$ and $P = -2\langle\rho\rangle k\dot{L}/L$. Using the equation of state $\langle P\rangle = \langle\rho\rangle RT$, the definition of the internal energy $\widetilde{U} = C_v\widetilde{T}$, and the specific heat ratio $\gamma = 5/3$, we have

$$\frac{d}{dt}\left(\widetilde{U} + k\right) = -2\widetilde{U}\frac{\dot{L}}{L} - 2k\frac{\dot{L}}{L}. \qquad (B4)$$

We note that the equation above corresponds to eq. (26) in [14]. Using Eqs. (B2) and (B4) in Eq. (B1), we can show that

$$\frac{d}{dt}\left(\frac{\widetilde{U} + k}{\widetilde{U}^{(a)}}\right) =$$
$$-2\widetilde{U}\frac{\dot{L}L}{\widetilde{U}_0} - 2k\frac{\dot{L}L}{\widetilde{U}_0} + 2\widetilde{U}\frac{L\dot{L}}{\widetilde{U}_0} + 2k\frac{L\dot{L}}{\widetilde{U}_0} = 0. \quad (B5)$$

---

[1] Z. Han and R. D. Reitz, "Turbulence modeling of internal combustion engines using RNG k-ϵ models," Combust. Sci. and Tech. **106**, 267–295 (1995).

[2] J. Larsson, I. Bermejo-Moreno, and S. K. Lele, "Reynolds- and Mach-number effects in canonical shock-turbulence interaction," J. Fluid Mech. **717**, 293–321 (2013).

[3] E. Kroupp, E. Stambulchik, A. Starobinets, D. Osin, V. I. Fisher, D. Alumot, Y. Maron, S. Davidovits, N. J. Fisch, and A. Fruchtman, "Turbulent stagnation in a Z-pinch plasma," Phys. Rev. E **97**, 013202 (2018).

[4] C. R. Weber, D. S. Clark, A. W. Cook, L. E. Busby, and H. F. Robey, "Inhibition of turbulence

in inertial-confinement-fusion hot spots by viscous dissipation," Phys. Rev. E **89**, 053106 (2014).

[5] B. M. Haines, F. F. Grinstein, and J. R. Fincke, "Three-dimensional simulation strategy to determine the effects of turbulent mixing on inertial-confinement-fusion capsule performance," Phys. Rev. E **89**, 053302 (2014).

[6] B. Robertson and P. Goldreich, "Adiabatic heating of contracting turbulent fluids," ApJ **750**, 2 (2012).

[7] C-T. Wu, J. H. Ferziger, and D. R. Chapman, *Simulation and modeling of homogeneous, compressed turbulence*, Ph.D. thesis, Stanford University (1985).

[8] G. N. Coleman and N. N. Mansour, "Modeling the rapid spherical compression of isotropic turbulence," Phys. Fluids A. **3**, 2255 (1991).

[9] G. A. Blaisdell, *Numerical simulation of compressible homogeneous turbulence*, Ph.D. thesis, Stanford University (1991).

[10] G. N. Coleman and N. N. Mansour, "Simulation and modeling of homogeneous compressible turbulence under isotropic mean compression," in *Turbulent Shear Flows 8*, edited by F. Durst *et al.* (Springer-Verlag, 1993).

[11] G. A. Blaisdell, G.N. Coleman, and N.N. Mansour, "Rapid distortion theory for compressible homogeneous turbulence under isotropic mean strain," Phys. Fluids **8**, 2692–2705 (1996).

[12] S. Davidovits and N. J. Fisch, "Sudden viscous dissipation of compressing turbulence," Phys. Rev. Lett. **116**, 105004 (2016).

[13] S. Davidovits and N. J. Fisch, "Compressing turbulence and sudden viscous dissipation with compression-dependent ionization state," Phys. Rev. E **94**, 053206 (2016).

[14] S. Davidovits and N. J. Fisch, "Modeling turbulent energy behavior and sudden viscous dissipation in compressing plasma turbulence," Phys. Plasmas **24**, 122311 (2017).

[15] G. Viciconte, B.-J. Gréa, and F. S. Godeferd, "Self-similar regimes of turbulence in weakly coupled plasmas under compression," Phys. Rev. E **97**, 023201 (2018).

[16] S. Davidovits and N. J. Fisch, "Bulk hydrodynamic stability and turbulent saturation in compressing hot spots," Phys. Plasmas **25**, 042703 (2018).

[17] D. C. Wilcox, *Turbulence Modeling for CFD*, 3rd ed. (DCW Industries, Inc., 2010).

[18] S. Kida and S. A. Orszag, "Energy and spectral dynamics in forced compressible turbulence," J. Sci. Comp. **5**, 85–125 (1990).

[19] S. K. Lele, "Compact finite difference schemes with spectral-like resolution," J. Comp. Phys. **103**, 16–42 (1992).

[20] C. A. Kennedy, Carpenter M. H., and R. M. Lewis, *Low-storage, explicit Runge-Kutta schemes for the compressible Navier-Stokes equations*, Tech. Rep.

99-22 (ICASE, 1999).

[21] C. R. Weber, D. S. Clark, A. W. Cook, D. C. Eder, S. W. Haan, B. A. Hammel, D. E. Hinkel, O. S. Jones, M. M. Marinak, J. L. Milovich, *et al.*, "Three-dimensional hydrodynamics of the deceleration stage in inertial confinement fusion," Phys. Plasmas **22**, 032702 (2015).

[22] C. R. Weber, A. W. Cook, and R. Bonazza, "Growth rate of a shocked mixing layer with known initial perturbations," J. Fluid Mech. **725**, 372–401 (2013).

[23] A. W. Cook, W. Cabot, and P Miller, "The mixing transition in rayleigh-taylor instability," J. Fluid Mech. **511**, 333–362 (2004).

[24] A. W. Cook, "Artificial fluid properties for large-eddy simulation of compressible turbulent mixing," Phys. Fluids **19**, 055103 (2007).

[25] B. J. Olson and J. Greenough, "Large eddy simulation requirements for the richtmyer-meshkov instability," Phys. Fluids **26**, 044103 (2014).

[26] M. R. Petersen and D. Livescu, "Forcing for statistically stationary compressible isotropic turbulence," Phys. Fluids **22**, 116101 (2010).

[27] A. Campos and B. Morgan, "The effect of artificial bulk viscosity in simulations of forced compressible turbulence," J. Comput. Phys. **371**, 111–121 (2018).

[28] S. B. Pope, *Turbulent Flows* (Cambridge University Press, 2000).

[29] H. Miura and S Kida, "Acoustic energy exchange in compressible turbulence," Phys. Fluids **7**, 1732–1742 (1995).

[30] S. Sarkar, "The pressure-dilatation correlation in compressible flows," Phys. Fluids A **4**, 2674–2682 (1992).

[31] C. Federrath, "On the universality of supersonic turbulence," MNRAS **436**, 1245–1257 (2013).

[32] L. Konstandin, W. Schmidt, P. Girichidis, T. Peters, R. Shetty, and R. S. Klessen, "Mach number study of supersonic turbulence: the properties of the density field," MNRAS **460**, 4483–4491 (2016).

[33] K. A. Flippo, F. W. Doss, E. C. Merritt, B. G. De-Volder, C. A. Di Stefano, P. A. Bradley, D. Capelli, T. Cardenas, T. R. Desjardins, F. Fierro, *et al.*, "Late-time mixing and turbulent behavior in high-energy-density shear experiments at high atwood numbers," Phys. Plasmas **25**, 056315 (2018).

[34] H. F. Robey, Y. Zhou, A. C. Buckingham, P. Keiter, B. A. Remington, and R. P. Drake, "The time scale for the transition to turbulence in a high reynolds number, accelerated flow," Phys. Plasmas **10**, 614 (2003).

[35] R. S. Rogallo, *Numerical Experiments in Homogeneous Turbulence*, Technical Memorandum 81315 (National Aeronautics and Space Administration, 1981).